Direct Quantification of Cu Vacancies and Spatial Localization of Surface Plasmon Resonances in Copper Phosphide Nanocrystals

Giovanni Bertoni,*[†‡] Quentin Ramasse,[§◊] Rosaria Brescia,[∥] Luca De Trizio,[‡] Francesco De Donato,[‡] Liberato Manna*[‡]

[†]CNR - Istituto Nanoscienze, Via Campi 213/A, 41125 Modena, Italy

[‡]Dept. Nanochemistry, Istituto Italiano di Tecnologia, Via Morego 30, 16163 Genova, Italy

[§]SuperSTEM, SciTech Daresbury Science and Innovation Campus, Keckwick Lane, Daresbury WA4 4AD, UK

[◊]School of Chemical and Process Engineering & School of Physics, University of Leeds, Leeds LS29JT, UK

[∥]Electron Microscopy Facility, Istituto Italiano di Tecnologia, Via Morego 30, 16163 Genova, Italy

ABSTRACT: Copper chalcogenides and pnictogenides often behave as heavily doped p-type semiconductors due to the presence of a high density of Cu vacancies, with corresponding hole carriers in the valence band. If the free carrier concentration is high enough, localized surface plasmon resonances can be sustained in nanocrystals of these materials, with frequencies that are typically observed in the infra-red region of the spectrum (<1 eV), differently from the typical resonances featured in the visible range by metallic nanoparticles. Here, we demonstrate that Cu vacancies in hexagonal $Cu_{3-x}P$ nanoplatelets can be directly quantified by scanning transmission electron microscopy (STEM) analysis. We also report for the first time the spatial localization of the plasmon resonances in individual $Cu_{3-x}P$ nanocrystals by means of STEM energy loss spectroscopy (EELS), an achievement that to date had been demonstrated only on nanoparticles of noble metals. Two plasmon modes can be seen from STEM-EELS, which are in agreement with the resonances calculated from the vacancy concentration obtained from the STEM analysis.

Nanostructures of heavily doped semiconductors, similarly to metallic nanoparticles, can exhibit plasmonic features deriving from the collective excitations of free carriers.[1,2] Among the various types of plasmonic semiconductor nanocrystals (NCs), copper-based binary compounds have received particular attention in recent years. Notable examples of these materials are colloidal NCs of copper chalcogenides ($Cu_{2-x}S$, $Cu_{2-x}Se$, and $Cu_{2-x}Te$).[3,4,5] The interest in these compounds stems from the fact that the density of free hole carriers in the valence band, hence the spectral position of the localized surface plasmon resonance (LSPR) is directly related to the density of copper vacancies. These, in turn, can be tuned by varying the synthesis conditions or by post-synthesis treatments.[6,7,8] An increasing density of Cu vacancies translates into a higher hole concentration, and consequently into a shift of the LSPRs toward higher frequencies. Pnictogenide $Cu_{3-x}P$ NCs also feature a band in the absorption spectrum, peaked at about 1500 nm, which has been recognized as a LSPR and attributed to the presence of Cu vacancies.[9,10,11] This LSPR in the near infra-red is of interest for application in the field of invisible optics in communication or energy harvesting.[12,13]

To unambiguously prove that the LSPR properties derive from the presence of Cu vacancies in the structure, a quantification of the Cu vacancies in the individual nanostructure is required. However, in copper chalcogenides, Cu^+ ions are highly mobile and therefore the sublattice of Cu^+ ions is highly disordered, which makes it difficult to visualize directly Cu vacancies with techniques such as scanning transmission electron microscopy (STEM). On the other hand, in $Cu_{3-x}P$ NCs the Cu vacancies are expected to be preferentially located at specific sites in the cell, which should make their visualization

and quantification possible. The first main achievement of the present work is indeed the direct quantification of the number of Cu vacancies per unit cell (n_V) in colloidally synthesized $Cu_{3-x}P$ hexagonal nanoplatelets, by means of STEM imaging. This is obtained by comparing the image contrast from the atomic columns in the experimental image with the contrast from quantum mechanical image simulations (using a multi-slice simulation algorithm).

The ability to image the spatial localization of the plasmonic resonances may then greatly assist in engineering these nanostructures for sensing and SERS.[13] The second main achievement of this work is thus the direct visualization of LSPRs in individual $Cu_{3-x}P$ nanoplatelets by means of electron energy loss spectroscopy (EELS). Although the visualization of LSPRs is now routinely performed in individual metallic nanostructures such as Ag and Au[14,15,16] and can be used to verify predictions from various models (Drude and Mie models, or boundary element methods, etc.),[17] it is still challenging in Cu-based chalcogenides, for two main reasons: a) the low cross-section of the electronic coupling with respect to the photon coupling in optical spectra, resulting in low signal to noise ratio; b) the low carrier density ($\sim 10^{20}$-10^{21} cm^{-3}), resulting in LSPR located at low energies,[1] usually in the infra-red, where the tail of the elastic peak (i.e., the zero-loss, or ZL peak) dominates the spectrum, resulting in low signal to background ratio. Several attempts have been made to study LSPRs in Cu-based semiconducting NCs by STEM-EELS.[18,19] However, the results so far were limited to average spectra, due to low signal to noise ratio, with no direct evidence of the localization of the resonances. In our $Cu_{3-x}P$ nanoplatelets, two
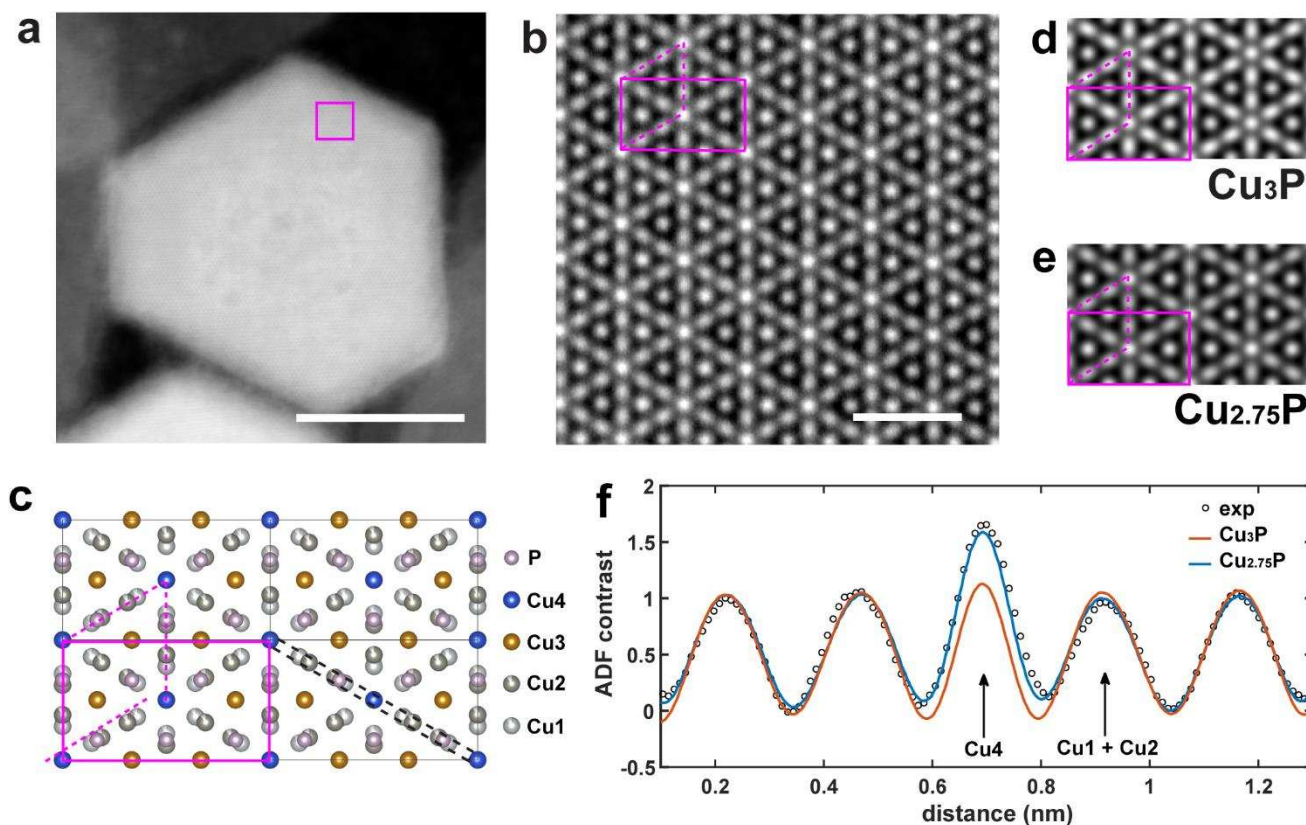
Figure 1. a) ADF-STEM image of a single $Cu_{3-x}P$ nanoplatelet. Scale bar 20 nm. b) High magnification image of the region indicated in a). The hexagonal P63cm unit cell (ICSD #15056) (purple dashed line) and the orthorhombic cell (purple solid line) used for simulation are indicated. Scale bar 1 nm. c) Plot of the P63cm structure, viewed along [001] zone-axis, with color codes for the inequivalent atoms. An occupancy f < 1 in Cu1 and Cu2 is indicated, while Cu3 and Cu4 have 1.0 occupancy. d-e) Simulated ADF-STEM images for the full stoichiometry Cu_3P (f = 1) and with f = 0.875 occupancy in Cu1 and Cu2 sites ($Cu_{2.75}P$), respectively. f) Integrated profile of intensity along the diagonal of the orthorhombic cell (dashed black profile in Figure 1c). The experimental data (open circles) are compared with the simulation with full stoichiometry (orange line) and with the 0.875 occupancy in Cu1 and Cu2 (blue line).

LSPRs modes could be unambiguously detected by STEM-EELS: a mode at about 0.6 eV and another one at about 0.8 eV. The two LSPR modes match with the two dominant modes from a boundary element simulation of the EELS probability, and based on a Drude model of the dielectric function, calculated from the experimentally measured vacancy density.

Synthesis of Nanoplatelets. In order to synthesize $Cu_{3-x}P$ nanoplatelets with a uniform size distribution we have developed a new colloidal approach which relies on the use of tris(diethylamino)phosphine as the phosphorous precursor (see the Experimental Methods section for details). The platelets had an average diameter d of 50 nm and an average thickness h of 10 nm. See Figure S1 in the Supporting Information (SI) for a representative low magnification TEM image of a collection of nanoplatelets.

Direct STEM imaging of Cu vacancies. The high-resolution annular dark-field STEM (ADF-STEM) image from a [001] projection of a single $Cu_{3-x}P$ NC is presented Figure 1a-b. A hexagonal structure compatible with $Cu_{3-x}P$ is visible. The atomic structure (ICSD #15056) is presented in Figure 1c, in which the not-equivalent Cu sites are indicated with different colors. In Figure 1d we display the simulated ADF image corresponding to 2×2 orthorhombic cells, obtained from a full Cu_3P stoichiometry with all Cu occupancies set to 1.0. As can

be seen from the image, the full stoichiometric structure does not match the contrast from the atomic columns in the experiment. In particular, the Cu1 and Cu2 atomic columns in the fully stoichiometric Cu_3P structure are too bright. Indeed, as previously calculated by density function theory (DFT), the probability of having a fully stoichiometric structure is low, as the vacancy formation energy (E_v) is negative for the Cu1 and Cu2 sites (and positive for the Cu3 and Cu4 sites).[10] According to these results, we lowered the occupancy of the Cu1 and Cu2 sites, while keeping that of the Cu3 and Cu4 sites at 1.0. A derivation of the estimate of the occupancy in Cu1 and Cu2 is described in more detail in Figure S2 in SI. An optimal match with the experiment was obtained with f = 0.875(12) occupancy, which corresponds to a $Cu_{2.75}P$ stoichiometry (Figure 1e). The contrast differences in the atomic columns with respect to full Cu stoichiometry is more evident from the integrated profile along the diagonal of the orthorhombic cell (Figure 1f). The occupancy of 0.875 for the Cu1 and Cu2 sites corresponds to x = 0.25, or 3.0 Cu vacancies in the orthorhombic cell (full line Figure 1b-e), or 1.5 in the hexagonal unit cell (dashed line). This observation further confirms the prediction of the presence of Cu vacancies in this system, as already found through DFT calculations and X-ray diffraction analyses reported in previous works.[9,10] (See also SI for PXRD analysis). The excellent agreement with compositional analy-

sis by energy-dispersive X-ray spectroscopy (Cu/P = 2.8, see SI) further proves the capability of STEM as a quantitative technique, if all the relevant parameters of the acquisition are well known.

Estimate of hole carriers and direct mapping of localized surface plasmons. The second step of the study was to visualize the LSPR modes inside a single $Cu_{3-x}P$ NC. Assuming that every vacancy generates a hole carrier ($n_h = n_V$), we expect n_h to be around $5.0 \cdot 10^{21}$ cm^{-3}, and in a hexagonal nanoplatelet, having d = 50 nm and h = 10 nm, this corresponds to ~10^5 hole carriers, which are enough to sustain a LSPR.[2] The LSPR of this material was observed to be at low energies, i.e. in the infra-red (around 0.8 eV), according to optical measurements.[9,10] For these reasons, we opted for DualEELS™ acquisition[21] (see the Experimental Methods section for details), in order to achieve a careful measurement of the position of the ZL peak as energy reference and, at the same time, good statistics in the plasmon region. To avoid damaging the structure with the electron beam during a long acquisition over the entirety of the NC, we intentionally limited the EEL spectrum image acquisition to a portion of the crystal, starting from the center of the hexagon and crossing the edge. Indeed, in insulators and semiconductors, areas of the sample not directly under electron illumination may be damaged, a process sometimes suggested to be phonon-mediated.[22] This could result in the creation of further vacancies and therefore a shift in the LSPR energies. Restricting the scanning area together with lowering the beam energy to 60 keV reduce this probability. The results from the spectrum image acquisition are presented in Figure 2.
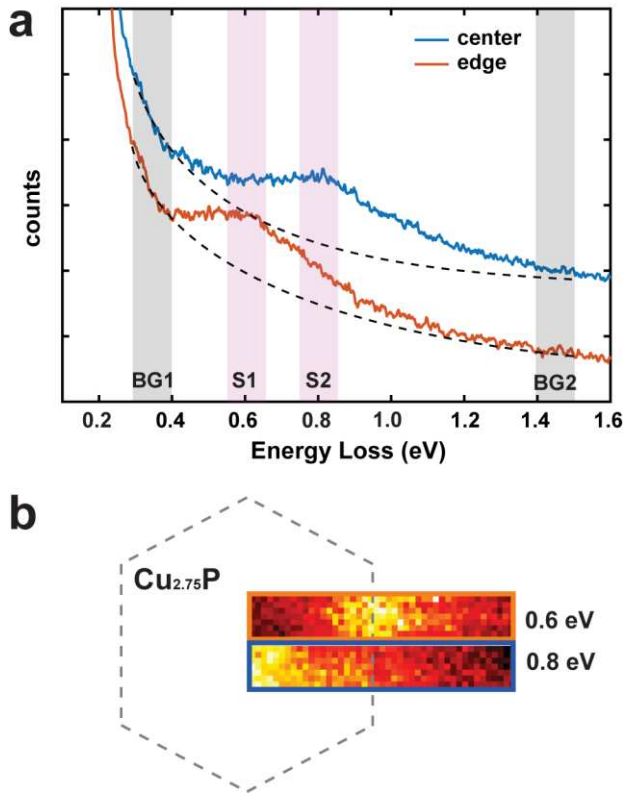

Figure 2. a) Representative EEL spectra from a $Cu_{3-x}P$ nanoplatelet. Two main resonances can be seen at the edge (orange line) and at the center of the crystal (blue line). All the background and

signal regions have 0.1 eV width. b) Intensity maps from the two resonances, obtained after background subtraction of a power-law function from the ZL peak tail, and extrapolated from the two fitting regions BG1 and BG2. The intensity maps refer to the integrated regions S1 and S2, respectively. The shape of the crystal is sketched with a dashed grey line.

Figure 2a shows two integrated spectra recorded at the center (blue curve) and at the edge (orange curve) of the NC. Two peaks are visible at approximately 0.6 eV and 0.8 eV, corresponding to two different LSPRs. Indeed, by subtracting a power-law background approximating the tail of the ZL peak, two intensity maps corresponding to the two LSPRs can be extracted (Figure 2b). The LSPR at 0.6 eV is located at the edge of the hexagon, while the LSPR at 0.8 eV is located at the center.

To further confirm the plasmonic nature of the two peaks, we performed a simulation of the EEL spectra and spectral maps using the boundary element method (MNPBEM17 Toolbox).[23] Unfortunately, the experimental dielectric constant $\varepsilon(E)$ for $Cu_{3-x}P$ is not available from the literature. For this reason, we built a Drude model, by calculating the plasmon (bulk) frequency from the estimated carrier density n_h, according to the formula:[24]

$$\omega_p = \sqrt{\frac{n_h e^2}{\varepsilon_0 m_h}}, \qquad \text{eq. 1,}$$
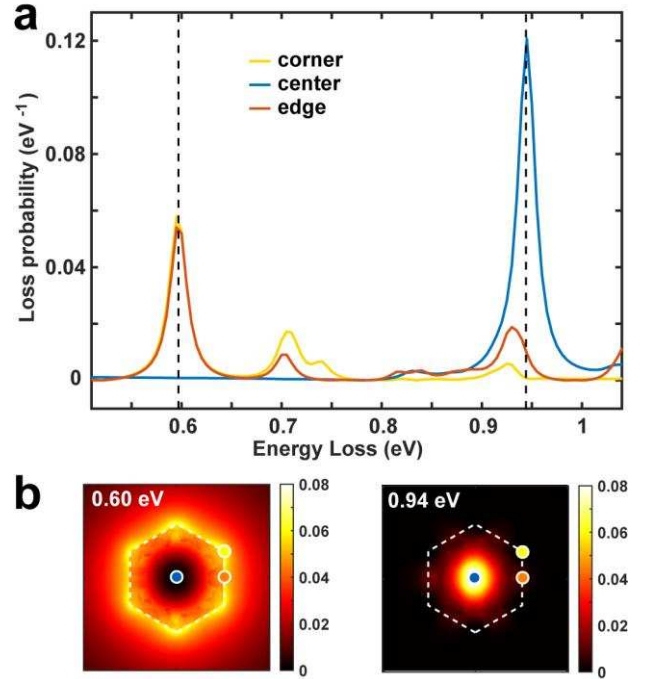
Figure 3. Simulated EEL spectra from the Drude model of the dielectric function in eq. 2. a) EEL spectra simulated at a corner, at the center, and at the edge of a $Cu_{2.75}P$ nanoplatelet. b) Corresponding intensity maps at the energy losses of the two peaks indicated in a) with dashed lines. The color circles correspond to the spatial positions for the spectra in a). The shape of the crystal is sketched with a dashed white line.

with ε_0 the vacuum permeability, e the electron charge, and m_h the hole mass ($m_h = 1.4\ m_0$).[9] The complex dielectric function $\varepsilon(E)$ was calculated as:[24]

$$\varepsilon(E) = 1 - \frac{\hbar^2 \omega_p^2}{E(E+i\gamma)} \qquad \text{eq. 2.}$$

The derived dielectric function was used as an input in the retarded simulation ($\gamma = 0.02$ eV). The results of the EELS simulation are reported in Figure 3. Figure 3a shows the loss probability measured at three different positions: at one corner of the hexagon, at the center, and at one edge. Figure 3b shows the corresponding intensity maps from the two peaks in the loss probability: two intense modes are visible, corresponding to the two peaks observed experimentally. The first one at 0.60 eV is localized at the edges and corners of the hexagon, while the one at 0.94 eV is located at the center. The two modes can be addressed as a dipolar and non-polar mode (or breathing mode) respectively,[25] by calculating the surface charge distributions (see Figure S7 in SI). To take into account the presence of the support film, the hexagon in the simulation was laid on a 3 nm thin amorphous carbon substrate (the nominal thickness of the ultrathin carbon grids in the experiment), and approximated with a square plate of 150 nm edge width. Retardation effects were included in the simulation, to account for the red shift of the peaks due to the substrate. It must be noted that, within a Drude model approximation, the simulated LSPRs are probably more intense than the real ones. Therefore, the simulation is to be intended for a sole qualitative comparison, and a more realistic model of the dielectric function would be needed to accurately match intensities and energy positions of the LSPR peaks. An estimated error in energy positions of the LSPRs of ±0.1 eV has to be considered, mainly deriving from the uncertainty in Cu occupancy from the ADF image contrast comparison. Nevertheless, the calculation is in very good agreement with the experimental findings, proving that LSPRs generated from hole carriers can be imaged in this system using EELS.

In summary, we have experimentally verified the presence of Cu vacancies in single semiconducting $Cu_{3-x}P$ NCs. From ADF-STEM images at atomic resolution, and in correlation with analytical energy-dispersive X-ray spectroscopy, we demonstrated that the Cu vacancies are located preferentially at the Cu1 and Cu2 sites as predicted from theory, resulting in a $Cu_{2.75}P$ composition. We also confirmed that the presence of Cu vacancies generates free hole carriers which can be collectively excited, resulting in two localized surface plasmon resonances in the infra-red region, as seen in the EELS maps acquired across the edge of the $Cu_{3-x}P$ NC. The two resonances match with the two modes calculated from a Drude model of the dielectric function based on the experimentally measured vacancy density.

EXPERIMENTAL METHODS

Chemicals. Copper chloride (CuCl, 99.999%) and tri-n-octylphosphine (TOP, min. 97%) were purchased from Strem Chemicals. Tris(diethylamino)phosphine (TDAP, 97%), Oleylamine (OLAM, 70%), 1-Octadecene (ODE, 90%), Chloroform anhydrous (CHCl3, $\geq$ 99%), 2-Propanol anhydrous ((CH3)2CHOH, 99.5%) were purchased from Merck.

Synthesis of $Cu_{3-x}P$ nanoplatelets. In a typical synthesis 1 mmol of CuCl (99 mg), 3 mL of OLAM and 6 mL of ODE were mixed in a 25 mL tri-neck flask. The solution was heated up to 120 °C and degassed at that temperature under vacuum. After 1 hour the solution was switched to Ar and the temperature was increased up to 260 °C. A solution of 0.9 mL of TOP and 0.164 mL of TDAP was swiftly injected inside the flask to trigger the nucleation of the NCs. The temperature was immediately set at 250 °C after the injection and the NC were allowed to grow at that temperature for 30 min. Eventually the reaction mixture was cooled down to room temperature and 5 mL of chloroform were added into the flask. The final solution was then transferred into a glass vial inside a N_2 filled glove box and the NCs were cleaned twice by dispersion in chloroform followed by precipitation by the addition of 2-propanol. The NCs were exposed to 1ml of OLAM and heated up to 80 °C for 1 hour in order to completely replace TOP on the surface with OLAM. This procedure assures that no phosphorous from the surfactant may interfere with the Cu:P quantification in EDXS. The resulting OLAM-capped NCs were precipitated by the addition of 2-propanol, eventually redispersed in 3 mL of Chloroform and stored in a glove box.

STEM imaging and image simulation. Atomic resolution images of the $Cu_{3-x}P$ NCs were acquired at 60 keV primary beam energy in annular dark field (ADF) STEM on a Nion UltraSTEM100 microscope, equipped with a probe aberration corrector (SuperSTEM, Daresbury, UK) and an Enfinium high resolution spectrometer (Gatan, Inc.). The convergence semi-angle was 31 mrad and the inner cutoff angle of the STEM detector 95 mrad. To achieve a higher signal to noise ratio and reduced drift distortions in the ADF image, several fast scans (> 20) were acquired and summed after cross correlation correction. For the simulation of the ADF image, we used the orthorhombic notation of the pristine hexagonal cell ($\mathbf{a'} = \mathbf{a}$, $\mathbf{b'} = 2\mathbf{b} - \mathbf{a}$, and $\mathbf{c'} = \mathbf{c}$). The hexagonal cell ($\mathbf{a}$, $\mathbf{b}$, $\mathbf{c}$) was taken from ICSD #15056 (P63cm, s.g. 185)[26] considering a = b = 0.6939 nm, and c = 0.7135 nm, as obtained from PXRD refinement (see SI). The ADF images were calculated using a multi-slice algorithm with the software DrProbe.[27] We took into account the finite size of the probe using a Gaussian profile of 100 pm width (FWHM). The atomic structure was drawn using VESTA.[28]

EELS spectrum imaging. Electron energy loss spectra (EELS), in the form of 3D (x, y, E) datasets (spectrum image) were acquired at 60 keV on the same machine by adjusting the slit position in the dispersion plane of the monochromator (ground potential monochromator),[29] resulting in a FWHM of the ZL peak of 0.024 eV (as a compromise between the highest achievable energy resolution and the resulting probe current and thus signal-to-noise ratio in the data). The acquisition at 60 keV reduces the retardation effects on the energy loss spectrum at low energy.[30,31] The spectra were acquired in DualEELS™ mode, enabling the acquisition of two simultaneous spectra on the CCD camera of the spectrometer. One spectrum (low-loss) contained the ZL peak acquired at short exposure (10 msec), while the other spectrum (high-loss) contained the region of the band-gap acquired at longer exposure (100 msec). The total acquisition time for the two spectra at one pixel was about 110 msec. The energy loss dispersion was fixed to 0.002 eV per channel. The low-loss spectrum was used to carefully align the spectra at sub-pixel level in the energy scale by fitting a Gaussian peak under the ZL peak. The result was applied to the corresponding high-loss spectra. We assumed no drift in the energy loss during the fast drift tube

change of the spectrometer from low-loss to high-loss region during the acquisition of a single pixel of the spectrum image. A thickness of the NCs was estimated from the EEL spectrum by using the log-ratio method and the approximation for the inelastic mean free path from Malis et al.[32] A thickness around 12 nm was obtained, which includes the contribution from the support film, and a relative error of 10% has to be considered.

EELS simulations. The simulation of the EEL spectra and energy loss maps were performed with the MNPBEM17 toolbox,[23] using the retarded approximation. A hexagonal platelet with rounded edges was used to approximate the shape of the NCs, and a thickness h = 10 nm was considered. A 3 nm thin square plate made of amorphous carbon with a constant dielectric function (n = 2.5)[33] was placed below the hexagonal platelet to approximate the presence of the ultrathin support carbon film of the TEM grid (see SI for further details).

EDXS quantification. Energy-dispersive X-ray spectroscopy (EDXS) was carried out on a Tecnai G^2 F20, equipped with a Bruker XFlash 6|T30 SDD system and an analytical sample holder. The sample suspension was drop-casted onto an ultrathin carbon coated Ni grid. Chemical quantification was carried out according to the Cliff-Lorimer ratio method.

ASSOCIATED CONTENT

Supporting Information. Cu vacancies estimation from ADF contrast, verification of Cu(I) valency, band gap determination, EDXS elemental quantification. This material is available free of charge via the Internet at http://pubs.acs.org.

AUTHOR INFORMATION

Corresponding Author

* giovanni.bertoni@nano.cnr.t, liberato.manna@iit.it

Author Contributions

The manuscript was written through contributions of all authors. / All authors have given approval to the final version of the manuscript.

Notes
The authors declare no competing financial interest.

ACKNOWLEDGMENT

ABBREVIATIONS

ADF, annular dark field; CCD, charge-coupled device; DFT, density functional theory, EELS, electron energy loss spectroscopy; EDXS, energy-dispersive X-ray electron spectroscopy; LSPR, localized surface plasmon resonance; NC, nanocrystal; PXRD, powder X-ray diffraction; SERS, surface-enhanced Raman spectroscopy; STEM, scanning transmission electron microscopy; ZL, zero-loss.

REFERENCES

(1) Agrawal, A.; Cho, S. H.; Zandi, O.; Ghosh, S.; Johns, R. W.; Milliron, D. J. Localized Surface Plasmon Resonance in Semiconductor Nanocrystals. Chem. Rev., **2018**, 118, 3121-3207.

(2) Luther, J. M.; Jain, P. K.; Ewers, T.; Alivisatos, A. P., Localized surface plasmon resonances arising from free carriers in doped quantum dots. Nat. Mater., **2011**, 10, 361-366.

(3) Dorfs, D.; Haertling, T.; Miszta, K.; Bigall, N. C.; Kim, M. R.; Genovese, A.; Falqui, A.; Povia, M.; Manna, L. Reversible Tunability of the Near-Infrared Valence Band Plasmon Resonance in Cu2-xSe Nanocrystals. J. Am. Chem. Soc., **2011**, 133, 11175-11180.

(4) Kriegel, I.; Jiang, C.; Rodríguez-Fernández, J.; Schaller, R. D.; Talapin, D. V.; da Como, E.; Feldmann, J. Tuning the Excitonic and Plasmonic Properties of Copper Chalcogenide Nanocrystals. J. Am. Chem. Soc., **2012**, 134, 1583-1590.

(5) Kriegel, I.; Rodríguez-Fernández, J.; Wisnet, A.; Zhang, H.; Waurisch, C.; Eychmüller, A.; Dubavik, A.; Govorov, A. O.; Feldmann, J. Shedding Light on Vacancy-Doped Copper Chalcogenides: Shape-Controlled Synthesis, Optical Properties, and Modeling of Copper Telluride Nanocrystals with Near-Infrared Plasmon Resonances. ACS Nano, **2013**, 7, 4367-4377.

(6) Garcia, G.; Buonsanti, R.; Runnerstrom, E. L.; Mendelsberg, R. J.; Llordes, A.; Anders, A.; Richardson, T. J.; Milliron, D. J. Dynamically Modulating the Surface Plasmon Resonance of Doped Semiconductor Nanocrystals. Nano Lett., **2011**, 11, 4415-4420.

(7) Xie, Y.; Riedinger, A.; Prato, M.; Casu, A.; Genovese, A.; Guardia, P.; Sottini, S.; Sangregorio, C.; Miszta, K.; Ghosh, S.; Pellegrino, T.; Manna, L. Copper Sulfide Nanocrystals with Tunable Composition by Reduction of Covellite Nanocrystals with Cu+ Ions. J. Am. Chem. Soc., **2013**, 135, 17630-17637.

(8) Marbella, L. E.; Gan, X. Y.; Kaseman, D. C.; Millstone, J. E. Correlating Carrier Density and Emergent Plasmonic Features in $Cu_{2-x}Se$ Nanoparticles. Nano Lett., **2017**, 17, 2414-2419.

(9) Manna, G.; Bose, R.; Pradhan, N. Semiconducting and Plasmonic Copper Phosphide Platelets. Angew. Chem. Int. Edit., **2013**, 52, 6762-6766.

(10) De Trizio, L.; Gaspari, R.; Bertoni, G.; Kriegel, I.; Moretti, L.; Scotognella, F.; Maserati, L.; Zhang, Y.; Messina, G. C.; Prato, M.; Marras, S.; Cavalli, A.; Manna, L. $Cu_{3-x}P$ Nanocrystals as a Material Platform for Near-Infrared Plasmonics and Cation Exchange Reactions. Chem. Mater., **2015**, 27, 1120-1128.

(11) Sun, T.; Wang, Y.; Yu, W.; Wang, Y.; Dai, Z.; Liu, Z.; Shivananju, B. N.; Zhang, Y.; Fu, K.; Shabbir, B.; Ma, W.; Li, S.; Bao, Q. Flexible Broadband Graphene Photodetectors Enhanced by Plasmonic $Cu_{3-x}P$ Colloidal Nanocrystals. Small, **2017**, 13, 1701881.

(12) Stanley, R. Plasmonics in the mid-infrared. Nat. Photon. **2012**, 6, 409–411.

(13) Sakamoto, M.; Kawawaki, T.; Kimura, M.; Yoshinaga, T.; Vequizo, J. J. M.; Matsunaga, H.; Ranasinghe, C. S. K.; Yamakata, A.; Matsuzaki, H.; Furube, A.; Teranishi, T. Clear and transparent nanocrystals for infrared-responsive carrier transfer. Nat. Comm. **2019**, 10, 406.

(14) Bosman, M.; Keast, V. J.; Watanabe, M.; Maaroof, A. I.; Cortie, M. B. Mapping surface plasmons at the nanometer scale with an electron beam. Nanotechnology, **2007**, 18, 165505.

(15) Nelayah, J.; Kociak, M.; Stephan, O.; Garcia de Abajo, F. J.; Tence, M.; Henrard, L.; Taverna, D.; Pastoriza-Santos, I.; Liz-Marzan, L. M.; Colliex, C. Mapping surface plasmons on a single metallic nanoparticle. Nat. Phys., **2007**, 3, 348-353.

(16) Scholl, J. A.; Koh, A. L.; Dionne, J. A. Quantum plasmon resonances of individual metallic nanoparticles. Nature, **2012**, 483, 421-427.

(17) Garcia de Abajo, F. J. Optical excitations in electron microscopy, Rev. Mod. Phys., **2010**, 82, 209-275.

(18) Casu, A.; Genovese, A.; Manna, L.; Longo, P.; Buha, J.; Botton, G. A.; Lazar, S.; Upadhyay, M.; Schwingenschlogl, U.; Prato, M.; Li, H.; Ghosh, S.; Palazon, F.; De Donato, F.; Mozo, S. L.; Zuddas, E.; Falqui, A. Cu_2Se and Cu Nanocrystals as Local Sources of Copper in Thermally Activated In-Situ Cation Exchange. ACS Nano, **2016**, 10, 2406-2414.

(19) Willhammar, T.; Sentosun, K.; Mourdikoudis, S.; Goris, B.; Kurttepeli, M.; Bercx, M.; Lamoen, D.; Partoens, B.; Pastoriza-Santos, I.; Perez-Juste, J.; Liz-Marzan, L. M.; Bals, S.; Van Tendeloo, G. Structure and vacancy distribution in copper telluride nanoparticles influence plasmonic activity in the near-infrared. Nat. Commun., **2017**, 8, 14925.

(20) Gaspari, R.; Labat, F.; Manna, L.; Adamo, C.; Cavalli, A. Semiconducting and optical properties of selected binary compounds by linear response DFT plus U and hybrid functional methods. Theor. Chem. Acc., **2016**, 135, 73.

(21) Scott, J.; Thomas, P. J.; MacKenzie, M.; McFadzean, S.; Wilbrink, J.; Craven, A. J.; Nicholson, W. A. P. Near-simultaneous dual energy range EELS spectrum imaging. Ultramicroscopy, **2008**, 108, 1586-1594.

(22) Kisielowski, C.; Specht, P.; Freitag, B.; Kieft, E. R.; Verhoeven, W., van Rens, J. F. M.; Mutsaers, P.; Luiten, J.; Rozeveld, S.; Kang, J.; McKenna, A. J.; Nickias, P.; Yancey, D. F. Adv. Funct. Mater. **2019**, 29, 1807818.

(23) Hohenester, U. Simulating electron energy loss spectroscopy with the MNPBEM toolbox. Comput. Phys. Commun., **2014**, 185, 1177-1187.

(24) Egerton R.F. Electron Energy-Loss Spectroscopy in the Electron Microscope, Third Edition, Springer, Boston, MA.

(25) Zanfrognini, M.; Rotunno, E.; Frabboni, S.; Sit, A.; Karimi, E.; Hohenester, U.; Grillo, V. Orbital Angular Momentum and Energy Loss Characterization of Plasmonic Excitations in Metallic Nanostructures in TEM. ACS Photonics, **2019**, 6, 620-627.

(26) Olofsson, O. Crystal-structure of Cu3P. Acta Chem. Scand., **1972**, 26, 2777-2787.

(27) Barthel, J. Dr. Probe: A software for high-resolution STEM image simulation. Ultramicroscopy, **2018**, 193, 1-11.

(28) Momma, K.; Izumi F. VESTA3 for three-dimensional visualization of crystal, volumetric and morphology data. J. Appl. Cryst. **2011**, 44, 1272-1276.

(29) Krivanek, O. L.; Ursin, J. P.; Bacon, N. J.; Corbin, G. J.; Dellby, N.; Hrncirik, P.; Murfitt, M. F.; Own, C. S.; Szilagyi, Z. S. High-Energy-Resolution Monochromator for Aberration-Corrected Scanning Transmission Electron Microscopy/Electron Energy-Loss Spectroscopy. Phil. Trans. R. Soc. A, **2009**, 367, 3683-3697.

(30) Stoeger-Pollach, M.; Franco, H.; Schattschneider, P.; Lazar, S.; Schaffer, B.; Grogger, W.; Zandbergen, H. W. Cerenkov losses: A limit for bandgap determination and Kramers-Kronig analysis. Micron, **2006**, 37, 396-402.

(31) Erni, R.; Browning, N. D. The impact of surface and retardation losses on valence electron energy-loss spectroscopy. Ultramicroscopy, **2008**, 108, 84-99.

(32) Malis, T.; Cheng, S. C.; Egerton, R. F. EELS log- ratio technique for specimen- thickness measurement in the TEM. J. Elec. Microsc. Tech., **1988**, 8, 193-200.

(33) Larruquert J. I.; Rodríguez-de Marcos L. V.; Méndez J. A.; Martin P. J.; Bendavid A. High reflectance ta-C coatings in the extreme ultraviolet, **2013** Opt. Express 21, 27537-27549.

For Table of Contents Only